Heavy-hole–light-hole exciton system in GaAs/AlGaAs quantum wells

M. N. Bataev ◎, M. A. Chukeev ◎, M. M. Sharipova, P. A. Belov ◎, P. S. Grigoryev ◎,[*] E. S. Khramtsov ◎, and I. V. Ignatiev ◎

Spin Optics Laboratory, St. Petersburg State University, Ulyanovskaya 1, Peterhof, St. Petersburg, 198504, Russia

S. A. Eliseev, V. A. Lovtcius ◎, and Yu. P. Efimov

Resource Center "Nanophotonics", St. Petersburg State University, Ulyanovskaya 1, Peterhof, St. Petersburg, 198504, Russia

Light-hole (lh) excitons (Xlhs) in quantum wells (QWs) are hardly studied compared with heavy-hole (hh) excitons (Xhhs), mainly due to the difficulties of their experimental observation. In this paper, a comprehensive study of both types of excitons in high-quality GaAs/AlGaAs QWs of different widths is performed. We focus on the energy positions of exciton resonances and the exciton-light interaction. The effect of mixing lhs and hhs in GaAs-based structures on these exciton characteristics is investigated. The corrections to the exciton energy due to mixing are only a fraction of millielectronvolts for wide QWs, in which the energy levels of Xhhs and Xlhs are close to each other. It is also experimentally found that the oscillator strength of Xlhs is ~2.5 times less than that of Xhhs. This value noticeably deviates from the 3:1 oscillator strength ratio known for optical transitions between free electron and hole states. This deviation originates from the different squeezing of the Xlh and Xhh wave functions due to distinct values of the effective masses of the Xlh and Xhh in the heterostructure. Mixing of hh and lh valence bands is not so important.

I. INTRODUCTION

Excitons in quantum wells (QWs) have been extensively studied for several decades since the publication by Dingle *et al.* [1]. In GaAs-based heterostructures, the valence band consists of the heavy-hole (hh) and light-hole (lh) subbands which are split in QWs. Correspondingly, the hh exciton (Xhh) and lh exciton (Xlh) can be observed in optical experiments. Xhhs have giant oscillator strength [2–4] and, therefore, have been extensively studied in experiments [5–10].

Much less is known about Xlhs [11–15]. Natural fundamental reasons for that are smaller oscillator strength and larger nonradiative broadening of Xlh resonances due to the phonon-mediated relaxation to the low-lying Xhh state. In wide QWs, the excited quantum-confined states of the Xhh overlap with the ground Xlh state, which complicates its identification and the study of coupling with light.

Exciton transitions are experimentally studied using photoluminescence (PL) or reflectance spectroscopy. The PL intensity from Xlhs is typically weak, at least for narrow QWs, in which Xlhs rapidly relax down to the Xhh state. Correspondingly, reliable determinations of Xlh energies and exciton oscillator strengths are problematic. Therefore, reflectance spectroscopy is mainly used for this purpose [15].

The exciton resonances observed in the reflectance spectra of high-quality heterostructures can be quantitatively described in the framework of the nonlocal optical response theory [3]. This theory allows one to precisely approximate the exciton resonance profile and to determine such characteristics of the Lorentz-shaped resonance as the exciton energy, the radiative and nonradiative broadenings, and the phase of the resonant reflection [5–8,15]. When the heterostructure is of moderate or poor quality, the inhomogeneous broadening of the exciton resonances can be considerably larger than the homogeneous one. In this case, the quantitative analysis of the resonances is complex and gives less reliable results.

This paper is devoted to an investigation of two particular issues in the Xhh-Xlh system, which have not been resolved yet. The first one is the role of hh-lh mixing in GaAs-based structures. The hh and lh states originate from the complex valence band and may be coupled. This coupling is theoretically described by the Luttinger Hamiltonian [3,16–18]. Experimentally, this coupling has been studied in many early works devoted to spectroscopy of excitons [11–13] as well as to quantum beats of the Xhh and Xlh and intervalence band coherence [19–24]. The quality of heterostructures at that time was not sufficient to draw certain conclusions about the role of coupling.

The second problem is exciton-light coupling. It can be quantitatively studied using the reflectance spectroscopy of the high-quality heterostructures, for which the inhomogeneous broadening of exciton resonances is negligibly small. The quantitative characteristics of the exciton-light coupling strength is the radiative broadening of exciton resonances $\hbar\Gamma_0$. It can be obtained from a reflectance spectrum by fitting the Lorentz-like resonance profile [3,15]. It is well known that, for the case of optical transition between free electron and hole states, the ratio of transition matrix elements electron (*e*) ↔ hh and *e* ↔ lh is 3:1 [3]. We could naively assume that this ratio is also valid for the exciton-light coupling constants

---

*philipp0grigoriev@gmail.com

(or oscillator strengths) for the Xhh and Xlh. This assumption deserves experimental verification for the high-quality heterostructures where resonant features for Xhh and Xlh transitions can be resolved in optical spectra.

In this paper, we have experimentally studied several high-quality GaAs/AlGaAs heterostructures with QWs of different widths and barrier heights. The energy positions of exciton resonances and the coupling constants $\hbar\Gamma_0$ for the Xhh and Xlh were experimentally obtained from the reflectance spectra measured for these structures.

We also theoretically calculated the energies and wave functions of several quantum-confined exciton states using two approaches. In the framework of a simplified approach, we numerically solved a three-dimensional Schrödinger equation, separately for the Xhh and Xlh, by the method described, e.g., in Refs. [6,7,10].

Within the second, more complicated approach, we solved the Schrödinger equation including the complete 4×4 Luttinger Hamiltonian and, hence, including coupling of the hh and lh subbands. The numerically obtained results were compared with the experimental data.

The major advantages of our results come from the narrow exciton resonances, i.e., from the high crystalline quality. Moreover, this is achieved by the nanostructure design intended to present resonances in a reflectance spectrum as narrow peaks to simplify the experimental data analysis. These advantages are based on our experience and the craftsmanship of the growth group. Significantly improved precision of experimental data is supported by the original theoretical approaches. Those include calculations involving modern computation facilities and sophisticated optimization of the numerical techniques.

II. EXPERIMENT

The structures under study were grown by the molecular beam epitaxy (MBE) on GaAs substrates with a crystallographic orientation (001). They contain GaAs QWs layers sandwiched between $Al_xGa_{1-x}As$ barrier layers characterized by various content of aluminum x. The most perfect structures were selected for this study. The criterion of the high quality is the negligible inhomogeneous broadening of exciton transitions compared with the homogeneous broadening.

The reflectance spectra of the structures are measured at the normal incidence of a probe light beam. The reflected beam is dispersed in a 0.5 m spectrometer with the 1800 gr/mm grating and detected using a nitrogen-cooled charge-coupled device array. The normalization of the detected signal on the light beam spectral profile is used to obtain the reflectance spectra of the sample.

Precise normalization of a reflectance spectrum is particularly accurate in this work. To obtain the absolute value of the reflectance, we used a monochromatic laser beam whose photon energy was tuned to a spectral point in the vicinity of an exciton resonance. The intensities of the incident and reflected beams were measured, and their ratio was used to calibrate the reflectance at the selected spectral point. The accuracy of this calibration is of $\sim 10\%$ considering some errors in the calibration of transparency and reflectance of several optical elements (cryostat windows, objective lenses,
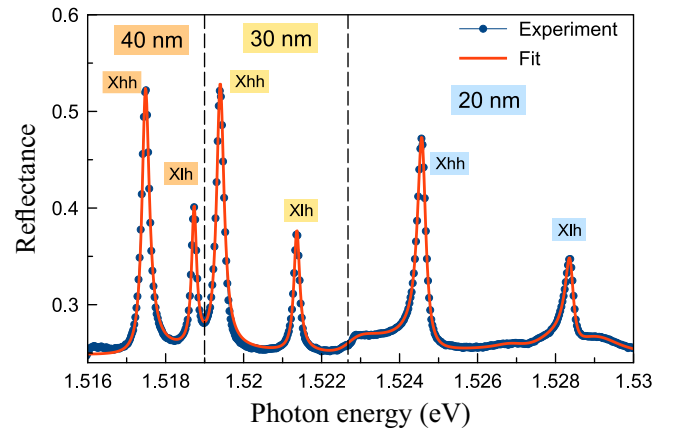

FIG. 1. Reflectance spectrum of heterostructure T844 with the 20, 30, and 40 nm $GaAs/Al_{0.16}Ga_{0.84}As$ quantum wells (QWs; points) and its fit by Eqs. (2) and (3) (solid curve). Labels Xhh and Xlh mark the lowest quantum-confined exciton states of heavy-hole and light-hole excitons, respectively, in each QW. Dashed lines divide regions with Xhh and Xlh resonances for 40, 30, and 20 nm QWs.

and mirrors) in the experimental setup. Unfortunately, the calibration of the whole reflectance spectrum has even larger error because the background reflection from the structure under study is modulated by the interference of the light waves reflected from different layers in the structure. This problem limits the accuracy of $\hbar\Gamma_0$ obtained from the experiment.

A typical reflectance spectrum of the structure T844 with three $GaAs/Al_xGa_{1-x}As$ QWs ($x = 0.16$) is shown in Fig. 1. It displays the Xhh and Xlh resonances in the spectral region of 1.518–1.530 meV. The resonances appear as peaks due to the appropriate choice of the top layer thicknesses. This thickness is chosen to fulfill a condition $L = N\lambda/2$ for each QW. Here, L is the distance from the sample surface to the middle for the QW, N is an integer number, and λ is the wavelength of light in the heterostructure. This condition defines the constructive interference of light reflected from the QW layer and from the sample surface.

The exciton resonances can be modeled in the framework of the nonlocal optical response theory described in a textbook by Ivchenko [3] and applied to the experimental data analysis in many works, see, e.g., Refs. [5–9,15]. The amplitude reflection coefficient of a QW r_j in the vicinity of a single exciton resonance is given by the expression:

$$r_j = \frac{i\Gamma_{0j}}{\omega_{0j} - \omega - i(\Gamma_j + \Gamma_{0j})}, \qquad (1)$$

where Γ_{0j} describes the radiative decay rate of the jth exciton state, Γ_j is the rate of the nonradiative relaxation from this state, and ω_{0j} is the frequency of the exciton transition j. These three quantities are considered fitting parameters of the model for each particular exciton resonance.

When a heterostructure contains several QWs, index j should numerate both the QWs (index l) and the quantum-confined exciton states (index k); thus, the index should be double $j = \{l, k\}$. To describe the excited quantum-confined
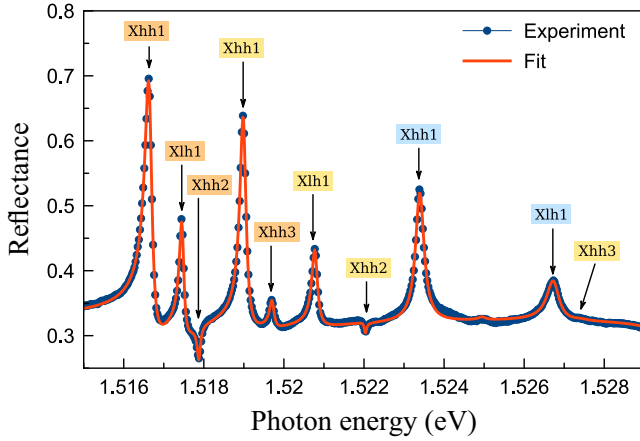
FIG. 2. Structure T846 with 22, 33, and 55 nm GaAs/Al$_{0.13}$Ga$_{0.87}$As quantum wells (QWs). In addition to the main resonances Xhh1 and Xlh1, several, less intense resonances Xhhk are identified with the use of the microscopic modeling (Sec. III A). Colors mark resonances belonging to different QWs: orange for the 55 nm QW, yellow for the 33 nm QW, and blue for the 22 nm QW.

states, Eq. (1) should be refined [5]:

$$r_j = \frac{i(-1)^{(k-1)}\Gamma_{0j}}{\omega_{0j} - \omega - i(\Gamma_j + \Gamma_{0j})}. \tag{2}$$

Factor $(-1)^{(k-1)}$ in the nominator of this equation comes from the symmetry of the exciton envelope wave function [3,5]. Its cross-section at the coinciding coordinates of the electron and the hole in the exciton has a cosinelike shape for the odd quantum-confined states ($k = 1, 3,..$) and a sinelike one for the even states ($k = 2, 4,..$). For the QWs with an asymmetric potential profile, an additional phase factor appears in the nominator of Eq. (2) [7]. Here, we consider only the symmetric rectangular QWs, which are well-proven models for the GaAs/AlGaAs heterostructures.

The total reflection depends also on the amplitude reflection coefficient of the sample surface r_s and can be expressed as

$$R = \left| \frac{r_s + \sum_j r_j \exp(i\phi_j)}{1 + r_s \sum_j r_j \exp(i\phi_j)} \right|^2, \tag{3}$$

where ϕ_j is the phase acquired by the light wave propagating from the sample surface to the middle of the jth QW layer. Phases ϕ_j are also considered fitting parameters because their values are very sensitive to small variations of the structure layer thicknesses [15].

Equations (2) and (3) are used to fit the spectra shown in Fig. 1. One can see that the calculated curves perfectly reproduce all peculiarities of the resonances. They describe the Lorentz-like profile of the resonances with slowly decaying wings. This is a clear evidence that no noticeable inhomogeneous broadening is present in the exciton system. Such broadening would result in the Gaussian-like wings characterized by a faster decay than the observed Lorentzian wings.

The good agreement of the experimental and calculated curves allows one to extract the main parameters of exci-
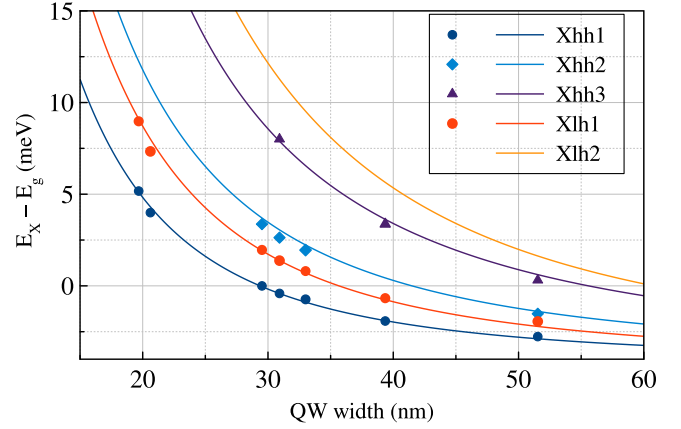

FIG. 3. Energies of the heavy-hole (Xhh) and light-hole (Xlh) excitons. Symbols are the experimental data taken from Figs. 1 and 2. Solid curves are the numerical calculations. $E_g = 1519.4$ meV [31].

ton resonances, the radiative ($\hbar\Gamma_{0j}$) and nonradiative ($\hbar\Gamma_j$) broadenings, as well as the exciton energy ($\hbar\omega_{0j}$) with an accuracy from a few microelectronvolts to fractions of microelectronvolts. Of course, some systematic uncertainties in the obtained values are also possible.

In addition to the main exciton resonances, which are easy to identify, there are several weak spectral peculiarities in Fig. 1. These weak resonances slightly deviate the background for the Xhh and Xlh resonances; therefore, we add them to the fitting curve. One of them is seen as a dispersion curve at ~ 1.5225 eV. In fact, there are two resonances: one comes in the form of a dip and another in the form of a peak. We assume them to be optical transitions to the second quantum-confined state for the 30 nm QW and the third state for the 40 nm QW, respectively. Their identification requires microscopic modeling of the exciton spectrum. Our further analysis present later in Fig. 3 confirms these assumptions.

The next example of the QW heterostructures is the sample T846 with three slightly wider QWs. Its reflectance spectrum is shown in Fig. 2. In this spectrum, in addition to the main resonances, several resonances observed as peaks or dips are clearly seen. Their identification based on the microscopic modeling (see the next section) is given in the figure. It is easy to see that the odd resonances (Xhh1, Xlh1, Xhh3, and Xhh5) are observed as peaks and the even ones (Xhh2) as dips. This rule directly follows from Eqs. (2) and (3), when the optical path from the sample surface to each QW is a multiple of a half-wavelength.

III. MICROSCOPIC MODELING OF EXCITON STATES

A. Simplified approach

The basic microscopic model of exciton states in QWs has been described in several preceding papers [6–8,10,25–27]. In this work, within the simplified approach, we have numerically solved a three-dimensional Schrödinger equation, separately for the Xhh and Xlh, in the rectangular QW. The width of the QW is varied in the range 10–100 nm. The depth of potential wells for electrons and holes is determined by the aluminum fraction in the barrier layers.

TABLE I. Material parameters for GaAs/Al$_x$Ga$_{1-x}$As heterostructures.

|	$x = 0.3$	$x = 0.15$
ΔE_g	365.52	172.905
V_e/V_h	$\frac{67}{33} \approx 2$	
	GaAs	AlAs
m_e	0.067	0.15
γ_1	6.98	3.76
γ_2	2.06	0.82
ε	12.53	10.06

FIG. 4. Differences of exciton energies as functions of the quantum well (QW) width. The value $dX = X_{\text{coupl}} - X_{\text{no}}$ is calculated as the difference between the exciton energy with coupling accounted and the energy of the uncoupled exciton state.

We have performed the calculations for the GaAs/Al$_{0.15}$Ga$_{0.85}$As heterostructures for the numerical and experimental data comparison. We used material parameters which are typically considered for the GaAs/AlGaAs heterostructures, see, e.g., [3,6,28,33]. They are listed in Table I. The notations are as follows: m_e is the effective mass of the electron in units of electron mass m_0; γ_1 and γ_2 are Luttinger's parameters; ΔE_g is the difference of bandgaps of the QW and barrier layers; and ε is the dielectric constant. The ratio of band offsets for the conduction and valence bands V_e/V_h is taken to be 2, which is close to the value in Ref. [33] ($V_e/V_h = \frac{65}{35}$). In the calculations, anisotropic hole effective masses were taken, as they are more appropriate for QWs with width <100 nm due to lifted degeneracy of the valence band. Additionally, the mass discontinuity at the QW interface is considered. It is proven that the mass discontinuity noticeably changes the exciton energies ($\delta E > 0.1$ meV) in the relatively narrow QWs ($L < 30$ nm). We neglected the nonparabolicity of electron dispersion and the discontinuity of dielectric constants of GaAs and Al$_{0.15}$Ga$_{0.85}$As layers, which cause a small effect on the exciton energies ($\delta E < 0.1$ meV) for QW widths $L > 10$ nm [18,29,30]. Details of the numerical procedure are described in Appendix.

Results of the calculations are shown in Fig. 3. The numerically obtained dependencies of exciton energies on the QW width L are approximated by a phenomenological function $y = a/(L^b + cL) + d$. The obtained parameters are listed in Appendix, Table II. The accuracy of the approximations is good, $\delta E \leqslant 0.1$ meV in the range $L = 10$–100 nm.

The experimental values of exciton energies extracted from Figs. 1 and 2 are shown in Fig. 3 by markers. Results obtained for one more structure (T867) with the 33 nm QW are also shown in this figure. As seen, the experimental and theoretical data agree well with each other. The typical deviation of all the experimental points from the calculated curves is only 0.3 meV. To minimize the deviation, we slightly scaled the QW layer thicknesses, particularly $L = 0.94 L_{\text{MBE}}$ for structure T846 and $L = 0.98 L_{\text{MBE}}$ for structure T844, where L_{MBE} is the value specified in the MBE program for these structures. This is due to a gradient in the layer thicknesses. The obtained agreement indicates that all valuable contributions are included in the microscopic calculations. The hh-lh subband mixing can slightly change the exciton energies. This effect is discussed in the next section.
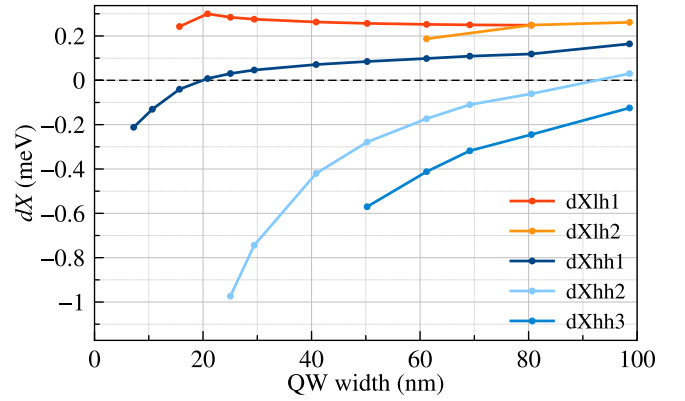
B. Model with hh-lh mixing

The hh-lh valence-band coupling is theoretically described by the Luttinger Hamiltonian [3,16]. It is a matrix of size 4×4; therefore, it considerably complicates the exciton Hamiltonian and the numerical solution of the respective Schrödinger equation. To make this problem solvable, we have considered the relative in-plane angular coordinate φ. Eigenfunctions of the angular momentum operator $\hat{k}_\varphi$ of the relative electon-hole motion in the exciton are used to represent the Luttinger Hamiltonian. For the diagonal part of the Hamiltonian, an angular momentum k_φ can be attributed as a quantum number. The hh-lh interaction couples exciton states with different k_φ according to the selection rules. Coupling occurs between the states, which k_φ differs by one or two. We consider therefore a restricted Hamiltonian including hh(lh) state with $k_\varphi = 0$ and three Xlh(Xhh) states with $k_\varphi = 1, 2, -2$ to describe bright Xhh(Xlh) states observed in the experiment. Thus, the matrix Hamiltonian, which includes hh-lh coupling, describes the superposition of four exciton states. This approach partially simplifies the numerical solution of the problem, but it remains too complex to be solved by a desktop computer. Further adaptation to available computational facilities was achieved by implementing a nonuniform grid for the discretization of the Hamiltonian operator. Details of the numerical procedure are described in Appendix. The nonuniform grid also allows one more accurate modeling of the exciton wave function at the coinciding coordinates of the electron and the hole. This is important for the calculations of exciton-light coupling (see the next section).

Like the calculations in the framework of the simplified approach, we have calculated energies of several quantum-confined states of the Xhh and Xlh as functions of the QW width. To highlight the effect of hh-lh coupling, we have calculated the exciton energies with allowance of coupling, X_{coupl} and without coupling X_{no}. Figure 4 shows the difference of these energies $dX = X_{\text{coupl}} - X_{\text{no}}$. As seen, hh-lh coupling shifts ground exciton states toward the higher exciton energies $dX < 0.3$ meV for the QW width $L > 20$ nm. This effect, however, is not governed by the energy distance between the

bright Xhh and Xlh states, which becomes small in wide QWs (see Fig. 3). According to the selection rules, it is rather governed by the distance between the bright observable state and dark states with nonzero angular momentum. Therefore, the coupling effect gets more pronounced for the lower QW widths $L < 20$ nm, where the Hamiltonian matrix elements defining the coupling become larger, while the distance between coupling states does not change significantly. This, however, is different for the ground lh state and the second hh state, which are drawn closer to the dark states with which they couple, and therefore, the coupling effect for those states gets more pronounced in thinner QWs.

For wider QWs, the coupling effect remains rather small and weakly changes since the distance between coupling states is mainly defined by the Coulomb interaction rather than the quantum-confined effect. The coupling states remain nondegenerate even in bulk materials, and hh-lh coupling changes the exciton energies in the 100 nm QW only slightly, as shown in our calculation.

IV. EXCITON-LIGHT COUPLING

The radiative decay constant Γ_0 can be calculated when the exciton wave function is obtained from microscopic modeling [3,26]:

$$\Gamma_0 = \frac{2\pi q}{\hbar \varepsilon} \left(\frac{e|p_{cv}|}{m_0 \omega_0} \right)^2 \left| \int_{-\infty}^{\infty} \Phi(z) \exp(iqz)\, dz \right|^2. \quad (4)$$

Here, $\Phi(z)$ is the cross-section of the exciton wave function with coinciding coordinates of the electron and the hole in the exciton. In the framework of the simplified approach, the cylindrical symmetry of the problem allows one to consider only three electron-hole coordinates: z_e and z_h are the electron and hole coordinates along the growth axis of the heterostructure, and ρ is the distance between the electron and the hole in the QW plane. The coincidence of the coordinates means: $z_e = z_h \equiv z$ and $\rho = 0$. Other notations in Eq. (4) are the following: $q = \sqrt{\varepsilon}\omega/c$ is the wave vector of light in the layer with dielectric constant ε, p_{cv} is the matrix element of the momentum operator between the electron and hole states, ω_0 is the exciton resonance frequency, and e and m_0 are the charge and free electron mass, respectively.

We have calculated the radiative decay rates for the ground Xhh and Xlh states using the simplified approach with the uniform and nonuniform grids as well as with allowance of Xhh-Xlh coupling. The effect of exciton coupling on the radiative decay rates is illustrated in Fig. 5. The upper panel in the figure shows the ratio of the radiative decay rates calculated with allowance of coupling (Γ_{0c}) and with no coupling (Γ_0), separately for the Xhh and Xlh. As seen from the figure, coupling decreases the radiative rates for wide QWs. This is the expected result since bright exciton states are coupled with dark ones, and originally, bright excitons become partially dark. However, coupling can also change the form of the exciton wave function, which results in the increase of the oscillator strength for the Xhh. At the same time, the anticrossing of the Xlh bright state with the Xhh dark states, in the vicinity of the 20 nm QW width, decreases the Γ_0 value of the Xlh state. For the Xhh state, coupling increases the Γ_0 value if the QW is thinner than 40 nm. All these effects, how-
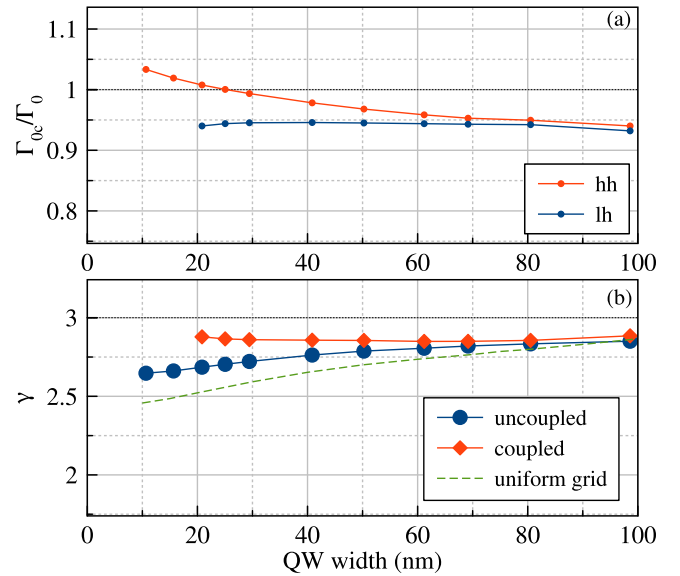

FIG. 5. (a) Effect of exciton coupling on the Xhh and Xlh decay rates. (b) Ratio of the radiative decay rates for the Xhh and Xlh calculated in different approaches.

ever, are relatively small comparing the experimental errors of the Γ_0 determination.

The lower panel of Fig. 5 presents the ratio of the Xhh radiative decay rate to that of the Xlh:

$$\gamma = \frac{\Gamma_{0hh}}{\Gamma_{0lh}}. \quad (5)$$

If the Xhh and Xlh would have the same envelope wave functions, this ratio would be exactly 3. This comes from the difference in the dipole matrix elements for the $e \to hh$ and $e \to lh$ transitions [3]. However, γ, which we obtained in all the approaches, substantially deviates from this value. Specifically, it gradually decreases with the QW width decrease.

The simplified approach with the uniform grid predicts the decrease from $\gamma = 2.84$ at $L = 100$ nm down to 2.45 at $L = 10$ nm. The calculations with the nonuniform grid predict similar dependence but slightly less pronounced. The dependence appears to be sensitive to coupling of the Xhh-Xlh states; however, the ratio remains below the expected value of 3. We can, therefore, conclude that the main origin of the lower value of γ is the difference of the envelope functions for the Xhh and Xlh.

Qualitative illustration of this difference is presented in Fig. 6. The figure presents wave function slices, with the exciton center of mass placed in the center of the 40 nm QW. As seen in the figure, the Xhh is more compact along the z axis than the Xlh. This is due to larger hole effective mass along this direction. These slices, however, are insufficient to describe the exciton-light interaction constant, as this value depends on how spread the wave function is. There are integral characteristics of the wave function that characterize this spread, namely, mean distances between the carriers along a given direction.

Using the numerically obtained wave functions, we calculated the mean electron-hole distances along the growth axis
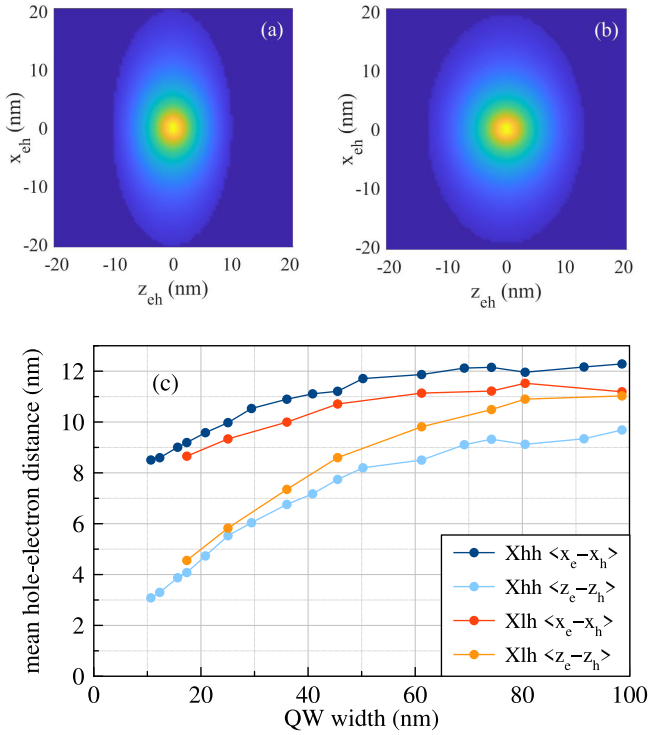
FIG. 6. Cross-sections of the envelope wave functions of the (a) Xhh and (b) Xlh in a 40 nm quantum well (QW) in coordinates $z_{eh} = z_e - z_h$ and $x_{eh} = x_e - x_h$. Axis x is directed along the QW layer. The center of mass of the excitons is in the middle of the QW. (c) Mean electron-hole distances in the z and x directions for the Xhh and Xlh for different QW widths.

and along one of the perpendicular axes. The mean distance is defined as

$$\langle \alpha_e - \alpha_h \rangle = \int \psi^* |\alpha_e - \alpha_h| \psi \, \rho \, dz_e dz_h d\rho. \qquad (6)$$

Numerical values of the wave functions on the grid were interpolated to obtain smooth function ψ. In the case of the x coordinate, the mean value of ρ was calculated, and then it was divided by $\sqrt{2}$ to account for the impact of the mean distance along the y coordinate in the $\langle \rho \rangle$ value. We employed the Monte Carlo technique to calculate the three-dimensional integrals. Calculation results are shown in the lower panel of Fig. 6. For the QW with widths $L < 40$ nm, the QW confinement mainly defines the electron-hole distance along the z direction, and the Xhh and Xlh reveal almost coinciding curves in the figure. The difference lies in the behavior of the exciton wave function perpendicular to the growth axis. As one can see, the electron and hole are closer in the Xlh; therefore, the exciton-light coupling constant acquires higher values. When combined with factor 3, arising from the interband transition probability, the Xhh to Xlh oscillator strength ratio becomes <3. The same analysis for the wider QWs cannot deliver such a clear argument. Still, calculations show that the ratio remains below the value of 3.

An additional factor controlling the behavior of γ in narrow QWs is penetration of the exciton wave function into the barrier layers. It is stronger for the Xlh that results in further increase of the overlap integral and in a decrease of γ. In
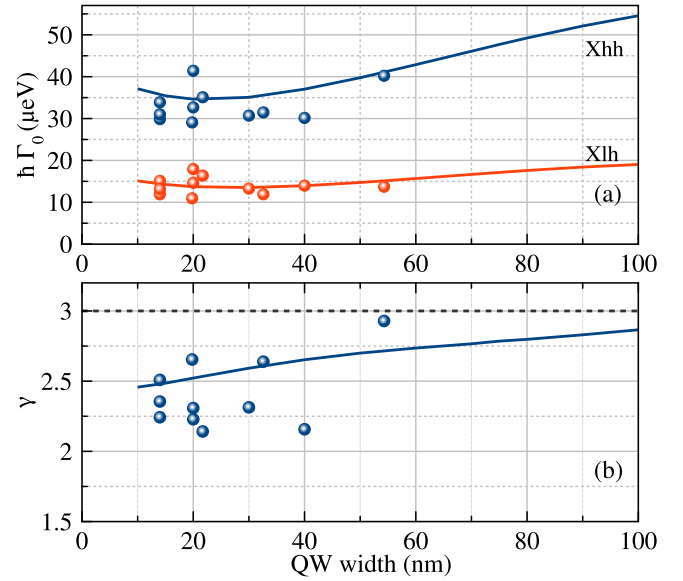

FIG. 7. (a) Radiative broadening constants $\hbar\Gamma_0$ for the heavy-hole (Xhh) and light-hole (Xlh) excitons (the lowest quantum-confined states) as functions of the quantum well (QW) width. (b) Ratio of the radiative constants for the Xhh and Xlh. Solid lines are the microscopic modeling (simplified approach). Symbols are the experimental data. The data obtained for other structures with the 14 and 20 nm QWs are also shown.

Fig. 6, one can see that electron-hole distance for the Xlh is indeed greater than that for the Xhh in the z direction, which illustrates the effect. However, our calculations show that this effect is less important than hh-lh coupling.

Figure 7 displays values of the radiative broadening of the Xhh and Xlh resonances extracted from the experiment for a series of samples. In addition to samples, for which spectra are present above, the data for samples with 14 and 20 nm QWs are shown in the figure. Although the measured radiative broadenings have a relatively large spread of their values, the ratio γ obtained experimentally is systematically <3. The ratio for the 55 nm QW substantially exceeds the value given by numerical modeling and reaches the value of 2.9. As seen in Fig. 2, the Xhh1 resonance for this QW is overlapped with a spectrally wide exciton resonance, which most probably comes from the wide GaAs buffer layer or substrate. The separation of these resonances would be a speculative procedure; therefore, we approximated these two resonances by a single exciton resonance. Therefore, we obtained a larger value for the Xhh1 radiative constant.

The absolute values of $\hbar\Gamma_0$ for the Xhh and Xlh, the ratio γ, and their dependence on the QW width are adequately described by the microscopic calculations in the framework of the simplified approach. It means that this approach is sufficient to describe the experiment within the unavoidable experimental errors.

There are several sources of the experimental errors. The main one is the small spectral features of background reflection r_s [see Eq. (3)]. They can be caused by the interference of light waves reflected from many technological layers in the heterostructure. The second important reason is the overlap of resonances related to the lowest exciton state in one QW with

those related to the excited states in other QWs and exciton states in technological layers and the substrate. Additionally, the sample surface can be covered by a thin layer of adsorbed molecules that changes the reflectance of the sample. All these spurious effects could be, in principle, minimized by the careful measurements of the background reflection near each exciton resonance (when it is possible) and by the modeling of the light interference as well as of the exciton states in the technological layers. However, for the structures containing several QWs as well as many technological layers, the modeling would be too complicated to give results with high enough accuracy. We should, however, emphasize that the error of the $\hbar\Gamma_0$ determination is of $\sim \pm 5\,\mu eV$, which is relatively small compared with the sum of the radiative and nonradiative broadenings of exciton resonances typically exceeding $100\,\mu eV$.

V. CONCLUSIONS

The experimental study of reflectance spectra of high-quality heterostructures with GaAs/AlGaAs QWs allowed us to identify several quantum-confined states of the Xhh and Xlh in the QWs of various widths. The observed exciton resonances were quantitatively analyzed, and the exciton transition energies were determined with high accuracy.

Microscopic modeling of exciton energies was performed using different approaches. It is found that the simplified approach considering the Xhh and Xlh as uncoupled subsystems describes well the energies and their dependencies on the QW width. The approximation formulas are suggested, which describe the numerically obtained dependencies with high accuracy. These formulas are useful for identification of exciton resonances in the newly grown structures.

The effect of Xhh-Xlh coupling on the exciton energies is also studied. It is shown that coupling results in the relatively small blueshift of the ground exciton state energy for the QW width $L > 20$ nm. For the narrower QW, it is larger and strongly dependent on the QW width.

The quantitative analysis of the exciton resonances also allowed us to extract the radiative broadening of the Xhh and Xlh transitions from the experiment. The ratio of the broadenings for the lowest Xhh and Xlh transitions is found to be systematically smaller than that predicted for optical transitions between free electron and hole states. Microscopic modeling shows that the main reason for this effect is the difference of effective masses of the Xhh and Xlh. Xhh-Xlh mixing is much less important.

ACKNOWLEDGMENTS

APPENDIX

1. Simplified approach

In the framework of the simplified approach, the hh and lh subbands are considered independent, and only the diagonal matrix elements of the Luttinger Hamiltonian are considered. The Hamiltonian for an exciton in a QW has a cylindrical symmetry, which considerably simplifies the solution of respective Schrödinger equations [6,10,25]. The basic equation of the problem has the form:

$$
\begin{aligned}
&\left[-\frac{\hbar^2}{2\mu_{jhxy}}\left(\frac{\partial^2}{\partial \rho^2} - \frac{1}{\rho}\frac{\partial}{\partial \rho} + \frac{1}{\rho^2} \right) \right. \\
&\left. -\frac{\hbar^2}{2m_e}\frac{\partial^2}{\partial z_e^2} - \frac{\hbar^2}{2m_{jhz}}\frac{\partial^2}{\partial z_h^2} - \frac{e^2}{\varepsilon\sqrt{\rho^2 + (z_e - z_h)^2}} \right. \\
&\left. + V_e(z_e) + V_h(z_h) \right]\chi = E\chi.
\end{aligned} \tag{A1}
$$

Here, the first term describes the kinetic energy of the relative electron-hole motion in the QW plane, where ρ is the electron-hole distance in the plane, and $\mu_{jhxy} = m_e m_{jhxy}/(m_e + m_{jhxy})$ is the exciton reduced mass. The second and third terms are, respectively, the kinetic energy of the electron and the hole across the QW layer. The next term is the Coulomb energy of the electron-hole interaction. The last two terms describe the potential wells for the electron and the hole. The hole mass is assumed to be anisotropic $m_{jhz} \neq m_{jhxy}$, where $j = h, l$ indicates the hh and lh. The hole masses are expressed via Luttinger parameters γ_1 and γ_2:

$$
\begin{aligned}
m_{hhz} &= \frac{m_0}{\gamma_1 - 2\gamma_2}, & m_{lhz} &= \frac{m_0}{\gamma_1 + 2\gamma_2}, \\
m_{hhxy} &= \frac{m_0}{\gamma_1 + \gamma_2}, & m_{lhxy} &= \frac{m_0}{\gamma_1 - \gamma_2}.
\end{aligned}
$$

The function $\chi(\rho, z_e, z_h) = \rho\psi(\rho, z_e, z_h)$, where $\psi(\rho, z_e, z_h)$ is the exciton wave function. The factor ρ is introduced in the definition of $\chi(\rho, z_e, z_h)$ to allow for zero boundary conditions at the coinciding coordinates of the electron and hole. Note that $\chi(\rho = 0) = 0$. The exponential decay of function χ for large values of the variables allows one to introduce zero boundary conditions for some cylindrical volume: $\chi(\rho = R_{max}) = 0$, $\chi(z_e = \pm L_{max}/2) = 0$, $\chi(z_h = \pm L_{max}/2) = 0$. Here, $L_{max} > L$ because the wave function can penetrate into the barrier layers.

2. Numerical realization

a. Differential operators

Differential operators in Eq. (A1) are replaced by finite-difference operators with accuracy $O(h^4)$ with constant step h. The functions $V_e(z_e)$, $V_h(z_h)$, and $e^2/[\varepsilon\sqrt{\rho^2 - (z_e - z_h)^2}]$ are replaced by the grid functions. The central finite-difference schemes are used for z_e, z_h, and ρ:

$$
\frac{\partial^2\chi}{\partial\rho^2} \approx \frac{-\chi_{-2} + 16\chi_{-1} - 30\chi_0 + 16\chi_1 - \chi_2}{12h^2} + O(h^4), \tag{A2}
$$

$$\frac{\partial \chi}{\partial \rho} \approx \frac{-3\chi_0 - 10\chi_1 + 18\chi_2 - 6\chi_3 + \chi_4}{12h} + O(h^4).$$

(A3)

Similar expressions are used for derivatives by z_e and z_h. For the first two ρ points, the expression reads

$$\frac{\partial^2 \chi}{\partial \rho^2} \approx \frac{10\chi_0 - 15\chi_1 - 4\chi_2 + 14\chi_3 - 6\chi_4 + \chi_5}{12h^2} + O(h^4).$$

(A4)

The Krylov-Schur method (based on the Arnoldi method) is used to find the first several eigenvalues and eigenfunctions numerically [32].

b. Extrapolation by step h

A desktop computer has a limited random access memory; therefore, the step cannot be chosen small enough to achieve desirable accuracy of calculations. A typical approach to the solution of this problem is the calculation of wave functions and energies for several gradually decreasing steps. In our case, the calculations are performed for the steps from 2 to 0.9 nm. Then extrapolation to the zero step is performed using the formula $y = ah^b + c$, where the fitting parameter b ranges from 1 to 2. The accuracy of the lowest exciton state energy obtained by the approximation is of $\sim 10\,\mu eV$. The excited quantum-confined exciton states with energies below the continuous spectrum are calculated with accuracy of $\sim 20\,\mu eV$. These numerical errors are still much less than possible errors related with inaccuracy of the GaAs and AlGaAs material parameters.

c. Extrapolation by magnetic field

High-energy quantum-confined exciton states can overlap with the continuous spectrum of states of electrons and holes moving along the QW layer. The algorithm we used cannot calculate the exciton states in this case. To solve this problem, we have applied a special method that allows us to make the continuous spectrum discrete [25,26], namely, terms describing the application of a magnetic field B along the z axis are introduced into the excitonic Hamiltonian. This magnetic field makes the states of free electrons and holes quantized (Landau levels). Thus, the continuous spectrum turns into a spectrum with discrete states. The variation of the magnetic field makes it possible to choose the case when the quantum-confined exciton states and the free electron and hole states differ in energy. The algorithm in this case can find the exciton states.

The magnetic field shifts the exciton states (diamagnetic shift). Therefore, to find proper states, we should calculate the states at different gradually decreasing values of the field B and then extrapolate the results to $B = 0$. In practice, the exciton states were calculated at $B = 0.5–7$ T. For each QW width and each exciton state falling into the continuous spectrum of states, particular values of magnetic field were slightly varied to obtain the maximum energy distance between the exciton state and the neighboring states of the free electron-hole pair. The extrapolation to zero magnetic field is fulfilled using a parabolic approximation of the exciton energies obtained

TABLE II. Fitting parameters of Eq. (A5) for aluminum concentration in the barriers $x = 0.15$.

Type	a	b	c	d	L_{low} (nm)	SD (μeV)
X_{hh1}	39 049	2.6242	88.97	−4.03	10	7
X_{hh2}	30 301	2.3481	39.78	−3.85	10	43
X_{hh3}	9464	1.9124	2.70	−4.07	20	57
X_{lh1}	73 264	2.6673	139.14	−3.94	10	12
X_{lh2}	550 000	2.8328	650.99	−3.67	10	25

at several values (typically 5–7) of B. The accuracy of the obtained exciton energies is better than 0.1 meV.

3. Approximation of the dependencies of the exciton energies on the QW width

Results of the microscopic calculations of the energies of exciton transitions for heterostructures GaAs/Al$_x$Ga$_{1-x}$As with aluminum content $x = 0.15$ and 0.30 were approximated by a phenomenological formula:

$$y = \frac{a}{L^b + cL} + d.$$

(A5)

The obtained values of fitting parameters are listed in Tables II and III. Since the calculation results were obtained in different intervals of L, the approximation was also made in different intervals with the low limit L_{low}, given in a separate column of the tables. The upper limit is the same $L_{upper} = 100$ nm. The standard deviation (SD) between the calculated points and the fitting curve is given in the last column.

4. Luttinger Hamiltonian representation in the chosen coordinate system.

The diagonal part of the Luttinger Hamiltonian given in Eq. (A1) assumes zero angular momentum. Considering the arbitrary angular momentum leads to the Hamiltonian:

$$\left[-\frac{\hbar^2}{2\mu_{jhxy}} \left(\frac{\partial^2}{\partial \rho^2} - \frac{1}{\rho}\frac{\partial}{\partial \rho} + \frac{1}{\rho^2} - \frac{k_\varphi^2}{\rho^2} \right) \right.$$
$$- \frac{\hbar^2}{2m_e}\frac{\partial^2}{\partial z_e^2} - \frac{\hbar^2}{2m_{jhz}}\frac{\partial^2}{\partial z_h^2} - \frac{e^2}{\varepsilon\sqrt{\rho^2 + (z_e - z_h)^2}}$$
$$\left. + V_e(z_e) + V_h(z_h) \right] \chi = E\chi.$$

(A6)

TABLE III. Fitting parameters of Eq. (A5) for aluminum concentration in the barriers $x = 0.3$.

Type	a	b	c	d	L_{low} (nm)	SD (μeV)
X_{hh1}	28 905	2.5294	14.30	−4.07	10	17
X_{hh2}	18 777	2.3481	39.78	−3.95	10	25
X_{hh3}	2526	1.6321	−2.49	−4.28	30	9
X_{hh4}	4.8716	1.0099	−1.03	−4.42	50	56
X_{lh1}	44 356	2.5211	52.21	−4.02	10	11
X_{lh2}	95 231	2.4020	58.09	−3.97	14	19
X_{lh3}	437	1.2607	−2.13	−4.70	60	33

The cubic symmetry of the 4×4 Luttinger Hamiltonian produces the angular dependence of the nondiagonal matrix elements in the chosen coordinate system. In the basis of the operator of angular momentum of the exciton internal motion, the Luttinger Hamiltonian is represented as an infinite matrix:

$$
\begin{pmatrix}
\ddots & & & \vdots & & & \\
& H_{hh,-1} & 0 & 0 & 0 & H_{31} & 0 & 0 & \\
& 0 & H_{lh,-2} & 0 & H'_{31} & 0 & 0 & & \\
& 0 & 0 & H_{lh,-1} & 0 & 0 & 0 & H'_{13} & \\
\cdots & 0 & H'_{13} & 0 & H_{hh,0} & H_{12} & H_{13} & 0 & \cdots \\
& H_{13} & 0 & 0 & H_{21} & H_{lh,1} & 0 & & \\
& 0 & 0 & 0 & H_{31} & 0 & H_{lh,2} & H_{21} & \\
& 0 & 0 & H'_{31} & 0 & 0 & H_{12} & H_{hh,1} & \\
& & & & \vdots & & & & \ddots
\end{pmatrix},
$$
$$(A7)$$

where in the diagonal terms, we use the subscript indexes denoting the types of effective masses and values of k_φ. Operators H_{12}, H_{13}, H'_{13}, H_{21}, H_{31}, and H'_{31} have the following form:

$$
H_{12} = i\frac{\sqrt{3}\gamma_3 \hbar^2}{m_0}\frac{\partial}{\partial z_h}\frac{\partial}{\partial \rho},
$$

$$
H_{21} = i\frac{\sqrt{3}\gamma_3 \hbar^2}{m_0}\left(-\frac{\partial}{\partial z_h}\frac{\partial}{\partial \rho} + \frac{1}{\rho}\frac{\partial}{\partial z_h}\right),
$$

$$
H_{13} = \frac{\sqrt{3}(\gamma_2 - \gamma_3)\hbar^2}{2m_0}\left(-\frac{1}{2\rho^2} - \frac{1}{2\rho}\frac{\partial}{\partial \rho} + \frac{1}{2}\frac{\partial^2}{\partial \rho^2}\right),
$$

$$
H_{31} = \frac{\sqrt{3}(\gamma_2 - \gamma_3)\hbar^2}{2m_0}\left(\frac{3}{2\rho^2} - \frac{3}{2\rho}\frac{\partial}{\partial \rho} + \frac{1}{2}\frac{\partial^2}{\partial \rho^2}\right),
$$

$$
H'_{13} = \frac{\sqrt{3}(\gamma_2 + \gamma_3)\hbar^2}{2m_0}\left(-\frac{1}{2\rho^2} - \frac{1}{2\rho}\frac{\partial}{\partial \rho} + \frac{1}{2}\frac{\partial^2}{\partial \rho^2}\right),
$$

$$
H'_{31} = \frac{\sqrt{3}(\gamma_2 + \gamma_3)\hbar^2}{2m_0}\left(\frac{3}{2\rho^2} - \frac{3}{2\rho}\frac{\partial}{\partial \rho} + \frac{1}{2}\frac{\partial^2}{\partial \rho^2}\right).
$$

We reduce the infinite Hamiltonian matrix to a restricted Hamiltonian with the diagonal part corresponding to the bright exciton states (with $k_\varphi = 0$) and those states that couple to them directly. For instance, for the hh subsystem, the Hamiltonian has the form:

$$
\hat{H} = \begin{pmatrix}
H_{hh,0} & H_{12} & H_{13} & H'_{13} \\
H_{21} & H_{lh,1} & 0 & 0 \\
H_{31} & 0 & H_{lh,2} & 0 \\
H'_{31} & 0 & 0 & H_{lh,-2}
\end{pmatrix}.
\qquad (A8)
$$

This restricted Hamiltonian is then transformed into the algebraic eigenvalue problem via the finite-difference method, which exploits the nonuniform grid described in the next subsection.

5. Numerical procedure for hh-lh mixing

To introduce hh-lh mixing into the numerical calculation, we had to optimize our numerical calculation beforehand. Thus, we implemented nonuniform grid in our calculation domain to decrease the number of grid nodes. For a $n_e \times n_h \times n_\rho = 120 \times 120 \times 120$ nm³ domain with 1 nm grid step, the Hamiltonian matrix would have been of $1\,728\,000 \times 1\,728\,000$ size. Here, n_e and n_h are the numbers of nodes along the z_e and z_h directions, respectively, and n_ρ is that along the ρ direction. When one implements a nonuniform grid, the

TABLE IV. Nonuniform grid parameters. All values are given in nanometers, except for grid dimensions, which are given in nodes. Here, $h_\rho = 1.64$ nm and $l_\rho = 2.2 \times 10^{-3}$ nm for 60 points along axis ρ, and $h_\rho = 0.66$ nm and $l_\rho = 2.3 \times 10^{-4}$ nm for 120 points along axis ρ.

QW	h_z	$l_z(10^{-4})$	Grid	Domain
10	0.66	3.5	$60 \times 60 \times 120$	$50 \times 50 \times 397$
12.5	0.82	4.4	$60 \times 60 \times 60$	$63 \times 63 \times 408$
15	0.82	4.4	$60 \times 60 \times 120$	$63 \times 63 \times 397$
17.5	0.82	4.4	$60 \times 60 \times 60$	$63 \times 63 \times 408$
20	0.82	4.4	$60 \times 60 \times 120$	$63 \times 63 \times 397$
25	0.98	5.3	$60 \times 60 \times 120$	$76 \times 76 \times 397$
30	0.98	5.3	$60 \times 60 \times 120$	$76 \times 76 \times 397$
35	0.98	3.9	$70 \times 70 \times 60$	$90 \times 90 \times 408$
40	0.99	3.9	$70 \times 70 \times 120$	$90 \times 90 \times 397$
45	0.99	3.4	$75 \times 75 \times 60$	$97 \times 97 \times 408$
50	0.99	3.0	$80 \times 80 \times 120$	$105 \times 105 \times 397$
60	0.99	3.0	$80 \times 80 \times 120$	$105 \times 105 \times 397$
70	0.99	2.6	$85 \times 85 \times 120$	$112 \times 112 \times 397$
75	0.99	2.4	$90 \times 90 \times 60$	$120 \times 120 \times 408$
80	0.99	2.4	$90 \times 90 \times 120$	$120 \times 120 \times 397$
90	0.99	1.6	$110 \times 110 \times 60$	$149 \times 149 \times 408$
100	0.99	1.4	$120 \times 120 \times 60$	$164 \times 164 \times 408$

number of nodes in such a domain can be reduced to $60 \times 60 \times 60$ points, shrinking the matrix almost eightfold by dimension. This allows us to add hh-lh coupling into consideration by simply representing the Luttinger Hamiltonian in the matrix form.

The nonuniform grid is defined by the polynomial smooth piecewise functions, defining coordinates of the nodes:

$$
z_i = \begin{cases}
ih_z + \left[\left(i - 5 - \frac{n}{2}\right)^3 - \left(5 - \frac{n}{2}\right)^3\right]l_z, \\
\quad \text{if } i > \frac{n}{2} + 5, \\
ih_z, \\
\quad \text{if } |i - \frac{n}{2}| < 5, \\
ih_z + \left[\left(i + 5 - \frac{n}{2}\right)^3 - \left(5 - \frac{n}{2}\right)^3\right]l_z, \\
\quad \text{if } i < \frac{n}{2} - 5,
\end{cases}
\qquad (A9)
$$

$$
\rho_i = \begin{cases}
ih_\rho, & \text{if } i < 8, \\
ih_\rho + (i - 8)^3 l_\rho, & \text{if } i \geqslant 8,
\end{cases}
\qquad (A10)
$$

where h_z, l_z, h_ρ, and l_ρ are constants defining the scale of linear and nonlinear parts of the grid, and $n = n_e = n_h$ is the number of nodes along the z coordinate. Constants 5 and 8 were arbitrarily chosen. The function in Eq. (A9) was used for z_e and z_h coordinates. Table IV lists the steps, grid sizes, and corresponding domains for each QW width for which the calculation was performed.

Difference schemes for the nonuniform grid were made like the schemes in Ref. [34]. For the schemes not present in that paper, a Taylor series expansion was employed to construct a system of linear equations defining scheme coefficients. We used the schemes with accuracy not worse than $\mathcal{O}(h^2)$, where h is the characteristic distance between nodes. The particular form of the differential operators was taken following Ref. [25], where a similar problem was solved for a wide InGaAs/GaAs QW.

It should be noted that, considering coupling demands high accuracy from the calculation. Indeed, the wave functions of states with angular momentum 1 that get mixed to the ground exciton states have two zeros along the ρ axis. To describe such functions accurately, one must use grids with smaller step size in the vicinity of the $\rho = 0$ point. In our calculation, a step <1 nm was required to achieve reliable results. On the other hand, in the region of higher ρ values, the wave function tends to exponentially decay. It does not oscillate, but having in mind zero boundary conditions in the calculation, it is necessary to set a larger domain in the ρ direction. Step size in this region can be larger. Our nonuniform grid approach meets both these requirements and allows one to reliably calculate the exciton wave function.

---

[1] R. Dingle, W. Wiegmann, and C. H. Henry, Quantum States of Confined Carriers in Very Thin AlGaAs-GaAs-AlGaAs Heterostructures, Phys. Rev. Lett. **33**, 827 (1974).

[2] B. Deveaud, F. Clèrot, N. Roy, K. Satzke, B. Sermage, and D. S. Katzer, Enhanced Radiative Recombination of Free Excitons in GaAs Quantum Wells, Phys. Rev. Lett. **67**, 2355 (1991).

[3] E. L. Ivchenko, *Optical Spectroscopy of Semiconductor Nanostructures* (Springer, Berlin, 2004).

[4] L. C. Andreani, F. Tassone, and F. Bassani, Radiative lifetime of free excitons in quantum wells, Solid State Commun. **77**, 641 (1991).

[5] A. V. Trifonov, S. N. Korotan, A. S. Kurdyubov, I. Ya. Gerlovin, I. V. Ignatiev, Y. P. Efimov, S. A. Eliseev, V. V. Petrov, Y. K. Dolgikh, V. V. Ovsyankin *et al.*, Nontrivial relaxation dynamics of excitons in high-quality InGaAs/GaAs quantum wells, Phys. Rev. B **91**, 115307 (2015).

[6] E. S. Khramtsov, P. A. Belov, P. S. Grigoryev, I. V. Ignatiev, S. Yu. Verbin, Y. P. Efimov, S. A. Eliseev, V. A. Lovtcius, V. V. Petrov, and S. L. Yakovlev, Radiative decay rate of excitons in square quantum wells: microscopic modeling and experiment, J. Appl. Phys. **119**, 184301 (2016).

[7] P. S. Grigoryev, A. S. Kurdyubov, M. S. Kuznetsova, I. V. Ignatiev, Y. P. Efimov, S. A. Eliseev, V. V. Petrov, V. A. Lovtcius, P. Yu. Shapochkin, Excitons in asymmetric quantum wells, Superlattices Microstruct. **97**, 452 (2016).

[8] E. S. Khramtsov, P. S. Grigoryev, D. K. Loginov, I. V. Ignatiev, Y. P. Efimov, S. A. Eliseev, P. Yu. Shapochkin, E. L. Ivchenko, and M. Bayer, Exciton spectroscopy of optical reflection from wide quantum wells, Phys. Rev. B **99**, 035431 (2019).

[9] A. V. Trifonov, E. S. Khramtsov, K. V. Kavokin, I. V. Ignatiev, A. V. Kavokin, Y. P. Efimov, S. A. Eliseev, P. Yu. Shapochkin, and M. Bayer, Nanosecond Spin Coherence Time of Nonradiative Excitons in GaAs/AlGaAs Quantum Wells, Phys. Rev. Lett. **122**, 147401 (2019).

[10] P. A. Belov, Energy spectrum of excitons in square quantum wells, Phys. E **112**, 96 (2019).

[11] W. T. Masselink, P. J. Pearah, J. Klem, C. K. Peng, and H. Morkoç, Absorption coefficients and exciton oscillator strengths in A1GaAs-GaAs superlattices, Phys. Rev. B **32**, 8027 (1985).

[12] R. T. Collins, L. Viña, W. I. Wang, L. L. Chang, and L. Esaki, Mixing between heavy-hole and light-hole excitons in GaAs/Al$_x$Ga$_{1-x}$As quantum wells in an electric field, Phys. Rev. B **36**, 1531 (1987).

[13] B. Gil, Y. El Khalifi, H. Mathieu, C. de Paris, J. Massies, G. Neu, T. Fukunaga, and H. Nakashima, Line-shape analysis of the reflectivity spectra of GaAs/(Ga,A1)As single quantum wells grown on (001)- and (311)-oriented substrates, Phys. Rev. B **41**, 2885 (1990).

[14] D. K. Loginov, E. V. Ubyivovk, Y. P. Efimov, V. V. Petrov, S. A. Eliseev, Y. K. Dolgikh, I. V. Ignat'ev, V. P. Kochereshko, and A. V. Sel'kin, Interference of polariton waves in structures with wide GaAs/AlGaAs quantum wells, Phys. Solid State **48**, 2100 (2006).

[15] P. Yu. Shapochkin, S. A. Eliseev, V. A. Lovtcius, and Yu. P. Efimov, P. S. Grigoryev, E. S. Khramtsov, and I. V. Ignatiev, Excitonic Probe for Quantum-State Engineering by MBE Technology, Phys. Rev. Appl. **12**, 034034 (2019).

[16] J. M. Luttinger, Quantum theory of cyclotron resonance in semiconductors: general theory, Phys. Rev. **102**, 1030 (1956).

[17] G. E. W. Bauer and T. Ando, Exciton mixing in quantum wells, Phys. Rev. B **38**, 6015 (1988).

[18] L. C. Andreani and A. Pasquarello, Accurate theory of excitons in GaAs-Ga$_{1-x}$Al$_x$As quantum wells, Phys. Rev. B **42**, 8928 (1990).

[19] K. Leo, T. C. Damen, J. Shah, E. O. Gobel, and K. Köhler, Quantum beats of light hole and heavy hole excitons in quantum wells, Appl. Phys. Lett. **57**, 19 (1990).

[20] B. F. Feuerbacher, J. Kuhl, R. Eccleston, and K. Ploog, Quantum beats between the light and heavy hole excitons in a quantum well, Solid State Commun. **74**, 1279 (1990).

[21] M. Koch, J. Feldmann, G. von Plessen, E. O. Gobel, P. Thomas, and K. Köhler, Quantum Beats versus Polarization Interference: An Experimental Distinction, Phys. Rev. Lett. **69**, 3631 (1992).

[22] J. Erland, D. Birkedal, V. G. Lyssenko, and J. M. Hvam, Spectral signatures of excitonic four-wave mixing signals in GaAs multiple quantum wells, J. Opt. Soc. Am. B **13**, 981 (1996).

[23] T. Meier, S. W. Koch, M. Phillips, and H. Wang, Strong coupling of heavy- and light-hole excitons induced by many-body correlations, Phys. Rev. B **62**, 12605 (2000).

[24] M. E. Donovan, A. Schülzgen, J. Lee, P.-A. Blanche, N. Peyghambarian, G. Khitrova, H. M. Gibbs, I. Rumyantsev, N. H. Kwong, R. Takayama *et al.*, Evidence for Intervalence Band Coherences in Semiconductor Quantum Wells via Coherently Coupled Optical Stark Shifts, Phys. Rev. Lett. **87**, 237402 (2001).

[25] P. S. Grigoryev, O. A. Yugov, S. A. Eliseev, Y. P. Efimov, V. A. Lovtcius, V. V. Petrov, V. F. Sapega, and I. V. Ignatiev, Inversion of Zeeman splitting of exciton states in InGaAs quantum wells, Phys. Rev. B **93**, 205425 (2016).

[26] P. S. Grigoryev, V. G. Davydov, S. A. Eliseev, Y. P. Efimov, V. A. Lovtcius, P. Yu. Shapochkin, I. V. Ignatiev, and M. Bayer, Exciton-light coupling in (In, Ga)As/GaAs quantum wells in longitudinal magnetic field, Phys. Rev. B **96**, 155404 (2017).

[27] P. A. Belov, Calculation of energy states of excitons in square quantum wells, Semiconductors **52**, 551 (2018).

[28] I. Vurgaftman, J. R. Meyer, and L. R. Ram-Mohan, Band parameters for III-V compound semiconductors and their alloys, J. Appl. Phys. **89**, 5815 (2001).

[29] V. A. Shuvayev, L. I. Deycha, I. V. Ponomarev, A. A. Lisyanskya, Self-consistent Hartree method for calculations of exciton binding energy in quantum wells, Superlattices Microstruct. **40**, 77 (2006).

[30] P. A. Belov and E. S. Khramtsov, The binding energy of excitons in narrow quantum wells, J. Phys.: Conf. Ser. **816**, 012018 (2017).

[31] The value of the bandgap we obtained is a bit larger than the value given in Ref. [28], $E_g = 1519$ meV. This difference is possibly due to a small mechanical stress present in GaAs/AlGaAs heterostructures.

[32] G. W. Stewart, A Krylov-Schur algorithm for large eigenproblems, SIAM J. Matrix Anal. Appl. **23**, 601 (2002).

[33] B. Gerlach, J. Wüsthoff, M. O. Dzero, and M. A. Smondyrev, Exciton binding energy in a quantum well, Phys. Rev. B **58**, 10568 (1998).

[34] J. Liu, G. A. Pope, K. Sepehrnoori, A high-resolution finite-difference scheme for nonuniform grids, Appl. Math. Model. **19**, 162 (1995).